Two-Fluid Flowing Equilibria of Helicity Injected Spherical Torus with Non-Uniform Density

Takashi KANKI, Loren C. STEINHAUER[1)] and Masayoshi NAGATA[2)]

Department of Maritime Science and Technology, Japan Coast Guard Academy, Kure, Hiroshima 737-8512, Japan
[1)]*University of Washington, Redmond Plasma Physics Laboratory, Redmond, Washington 98052, USA*
[2)]*Department of Electrical Engineering and Computer Sciences, University of Hyogo, Himeji, Hyogo 671-2201, Japan*

(Received 8 November 2007 / Accepted 19 March 2008)

Two-dimensional two-fluid flowing equilibria of helicity-injected spherical torus with non-uniform density and both toroidal and poloidal flows for each species have been numerically determined by the nearby-fluids procedure. It is found from the numerical results that the equilibrium for the driven λ ($\equiv \mu_0 \boldsymbol{j} \cdot \boldsymbol{B}/B^2$) profile exhibits a diamagnetic toroidal field, high-β (toroidal beta value, $\beta_t = 32\%$), hollow current profile, and centrally broad density. In contrast, the decaying equilibrium exhibits a paramagnetic toroidal field, low-β ($\beta_t = 10\%$), centrally peaked current profile, and density with a steep gradient in the outer edge region. In the driven case, the toroidal ion and electron flows are in the same direction, and two-fluid effects are less important since the $\boldsymbol{E} \times \boldsymbol{B}$ drift is dominant. In the decaying case, the toroidal ion and electron flows are opposite in the outer edge region, and two-fluid effects are significant locally in the edge due to the ion diamagnetic drift.

Keywords: helicity injection, equilibrium, plasma flow, two-fluid effect, $\boldsymbol{E} \times \boldsymbol{B}$ drift, diamagnetic drift

DOI: 10.1585/pfr.3.S1066

1. Introduction

Many experiments on the current drive of a spherical torus using a coaxial helicity injection (CHI) have been performed to elucidate the current drive mechanism for CHI. In these experiments, $\boldsymbol{E} \times \boldsymbol{B}$ plasma toroidal rotation with an $n = 1$ kink mode during CHI has been observed. It is recognized that the effect of plasma flow is important in understanding the confinement and relaxed states of helicity-injected spherical torus (HI-ST) plasmas. In particular, in the Helicity Injected Torus-II (HIT-II) experiments, a rotating $n = 1$ magnetic structure observed at the outer plasma edge is locked to the electron fluids and not to the ion fluids, suggesting a rotating magnetic field current drive [1]. Because of this behavior, the equilibrium computation of HI-ST plasmas must consider two-fluid effects [2, 3]. The formalism for two-fluid flowing equilibria was developed [4], and two-dimensional equilibria in helicity-driven systems using the two-fluid model were previously computed, showing the existence of an ultra-low-q spherical torus configuration with diamagnetism and higher beta [5]. However, this computation assumed purely toroidal ion flow and uniform density. The purpose of this study is to apply the two-fluid model to the two-dimensional equilibria of HI-ST with non-uniform density and both toroidal and poloidal flows for each species by the nearby-fluids procedure [6], and to explore their properties. We focus our attention on the equilibria relevant to the Helicity Injected Spherical Torus (HIST) device, which are characterized by either driven or decaying λ ($\equiv \mu_0 \boldsymbol{j} \cdot \boldsymbol{B}/B^2$) profiles [7]. Here μ_0, $\boldsymbol{j}$, and $\boldsymbol{B}$ are the permeability of vacuum, current density, and magnetic field, respectively. We have qualitatively reproduced the HIST equilibria in the driven or decaying λ profiles on the basis of experimental data such as λ, $\boldsymbol{j}$, and $\boldsymbol{B}$ profiles. In Sec. 2, we describe the governing equations and boundary conditions for a flowing two-fluid equilibrium. The numerical results are presented in Sec. 3, followed by summary and conclusions in Sec. 4.

2. Governing Equations and Boundary Conditions

Let us assume axisymmetry about the HIST geometric axis (see Fig. 4 (a)) in cylindrical coordinates (r, θ, z). Using dimensionless variables, an axisymmetric two-fluid flowing equilibrium can be described by a pair of generalized Grad-Shafranov equations for ion surface variable Y and electron surface variable ψ [6],

$$\bar{\psi}_i' r^2 \nabla \cdot \left(\frac{\bar{\psi}_i'}{n} \frac{\nabla Y}{r^2} \right) = \frac{r}{\varepsilon} \left(B_\theta \bar{\psi}_i' - n u_\theta \right) + n r^2 \left(H_i' - T_i S_i' \right), \tag{1}$$

$$r^2 \nabla \cdot \left(\frac{\nabla \psi}{r^2} \right) = \frac{r}{\varepsilon} \left(B_\theta \bar{\psi}_e' - n u_\theta \right) - n r^2 \left(H_e' - T_e S_e' \right), \tag{2}$$

and a generalized Bernoulli equations for the density n,

$$\frac{\gamma}{\gamma - 1} n^{\gamma - 1} \exp\left[(\gamma - 1) S_i \right] + \frac{u^2}{2} + \phi_E = H_i, \tag{3}$$

author's e-mail: kanki@jcga.ac.jp

$$\frac{\gamma}{\gamma-1}n^{\gamma-1}\exp\left[(\gamma-1)S_{\rm e}\right]-\phi_E=H_{\rm e}. \tag{4}$$

Here $\boldsymbol{u}$, T_α, ϕ_E, and γ are the ion flow velocity, species ($\alpha=$ i, e) temperature, electrostatic potential, and adiabatic constant, respectively. In addition, the two-fluid parameter $\varepsilon=\ell_{\rm i}/R$ measures the ion skin depth $\ell_{\rm i}=\sqrt{m_{\rm i}/(\mu_0 ne^2)}$ (R, $m_{\rm i}$, and e are the radius of the flux conserver (FC) used in HIST ($R=0.5$ m), ion mass, and electron charge, respectively). The two-fluid parameter $\varepsilon=0.0625$ is given by using $n=5.0\times10^{19}$ m^{-3} obtained in the HIST experiment, and the value of γ is assumed as 5/3 in the computation. Note that ψ corresponds to the familiar poloidal flux function. The poloidal flow stream function $\bar{\psi}_\alpha$, total enthalpy function H_α, and entropy function S_α are arbitrary surface functions of their respective surface variables. The three arbitrary functions $\Lambda_\alpha(\equiv\bar{\psi}'_\alpha)$, H_α, and S_α for each species can be assumed to reflect λ, $\boldsymbol{j}$, and $\boldsymbol{B}$ profiles on the basis of the experimental data by choosing appropriate function forms,

$$\Lambda_{\rm i}({\rm Y})=\Lambda_{\rm i0}+(\Lambda_{\rm i1}-\Lambda_{\rm i0})\left.\frac{{\rm d}f}{{\rm d}x}\right|_{Y-\Delta Y;\delta_{\rm i1},\delta_{\rm i2}}, \tag{5}$$

$$\Lambda_{\rm e}(\psi)=\Lambda_{\rm e0}+(\Lambda_{\rm e1}-\Lambda_{\rm e0})\left.\frac{{\rm d}f}{{\rm d}x}\right|_{\psi-\Delta\psi;\delta_{\rm e1},\delta_{\rm e2}}, \tag{6}$$

$$f(x;\delta_1,\delta_2)=\frac{1}{\delta_1+\delta_2}\times\left\{\begin{array}{ll}\delta_1^2\exp[x/\delta_1]; & x<0\\ \delta_1 x+\delta_2\sqrt{\delta_2^2+x^2-\delta_2^2+\delta_1^2}; & x\geq0\end{array}\right\}. \tag{7}$$

Here $\Lambda_{\alpha0}$, $\Lambda_{\alpha1}$, $\delta_{\alpha0}$, $\delta_{\alpha1}$, ΔY, and $\Delta\psi$ are constant parameters. By adjusting these constant parameters, we can obtain the driven or decaying λ profiles obtained in the HIST experiment. In the driven plasma case, $\Lambda_{\rm e0}$ is larger than $\Lambda_{\rm e1}$, while in the decaying plasma case, $\Lambda_{\rm e0}$ is smaller than $\Lambda_{\rm e1}$. Similarly, other arbitrary functions H_α and S_α are defined as follows:

$$H_{\rm i}({\rm Y})=H_{\rm i0}+(H_{\rm i1}-H_{\rm i0})\left.\frac{{\rm d}f}{{\rm d}x}\right|_{Y-\Delta Y_{Hi};\delta_{Hi1},\delta_{Hi2}}, \tag{8}$$

$$H_{\rm e}(\psi)=H_{\rm e0}+(H_{\rm e1}-H_{\rm e0})\left.\frac{{\rm d}f}{{\rm d}x}\right|_{\psi-\Delta\psi_{He};\delta_{He1},\delta_{He2}}, \tag{9}$$

$$S_i({\rm Y})=S_{\rm i0}+(S_{\rm i1}-S_{\rm i0})\left.\frac{{\rm d}f}{{\rm d}x}\right|_{Y-\Delta Y_{Si};\delta_{Si1},\delta_{Si2}}, \tag{10}$$

$$S_{\rm e}(\psi)=S_{\rm e0}+(S_{\rm e1}-S_{\rm e0})\left.\frac{{\rm d}f}{{\rm d}x}\right|_{\psi-\Delta\psi_{Se};\delta_{Se1},\delta_{Se2}}. \tag{11}$$

Here $H_{\alpha0}$, $H_{\alpha1}$, $\delta_{H\alpha0}$, $\delta_{H\alpha1}$, ΔY_{Hi}, $\Delta\psi_{He}$, $S_{\alpha0}$, $S_{\alpha1}$, $\delta_{S\alpha0}$, $\delta_{S\alpha1}$, ΔY_{Si}, and $\Delta\psi_{Se}$ are constant parameters.

Equations (1) and (2) have terms of order $1/\varepsilon$ on the right-hand side, which cause singularities. We employ the nearby-fluids procedure to eliminate the singularities [6]. This procedure requires that the two arbitrary functions $\Lambda_{\rm i}$ and $\Lambda_{\rm e}$ must differ only in $O(\varepsilon)$. We consider replacing these two arbitrary functions with a pair of arbitrary functions F and G expressed as follows:

$$\Lambda_{\rm e}(\psi)=F(\psi),\quad \Lambda_{\rm i}({\rm Y})=F({\rm Y})+\varepsilon G'({\rm Y}). \tag{12}$$

Note that G and $\Lambda_{\rm e}$ are related to the toroidal field function and the familiar Taylor $\lambda(\psi)$ function, which is usually used in a force-free relationship, $\boldsymbol{j}=\lambda(\psi)\boldsymbol{B}$, respectively. From Eq. (12), G is given as

$$G({\rm Y})=G_0+\frac{1}{\varepsilon}\int(\Lambda_{\rm i}(Y)-\Lambda_{\rm e}(Y))\,{\rm d}Y. \tag{13}$$

The parameter G_0 includes the effect of a vacuum toroidal field $B_{{\rm t}.v}$ produced by a toroidal field coil current along the geometry axis inside the central conductor. The experimentally typical $B_{{\rm t}.v}$ of 0.135 T on $R_0=(R_{\rm c}+R)/2$, which corresponds to G_0 of 1.5 is used in the computation, where $R_{\rm c}$ is the radius of the central conductor ($R_{\rm c}=0.05715$ m). Note that the toroidal field with $\Lambda_{\rm e}<\Lambda_{\rm i}$ results in a paramagnetic profile, while that with $\Lambda_{\rm e}>\Lambda_{\rm i}$ results in a diamagnetic one.

Next, we consider the boundary conditions [8–10] for Eqs. (1)-(4). No magnetic flux penetrates the FC, central conductor, and entrance port of the FC. Therefore, ψ is fixed at 0 at the FC wall and surface of the central conductor and entrance port. The bias flux is given by assigning fixed values of ψ to grid points corresponding to the left open end. These values are calculated using the formula,

$$\psi_{\rm bias}(r)=\frac{4\psi_{\rm s}}{(R_{\rm e}-R_{\rm c})^2}(r-R_{\rm c})(R_{\rm e}-r), \tag{14}$$

where $R_{\rm e}$ and $\psi_{\rm s}$ are the radius of the entrance port ($R_{\rm e}=0.19$ m) and the maximum value of the bias flux, respectively. The experimentally typical $\psi_{\rm s}$ of 2.36 mWb, which corresponds to the dimensionless value of 0.03, is used in the computation. Under the above assumptions and boundary conditions, the equilibrium is numerically determined by a successive over-relaxation method for updating the poloidal flux function ψ and a Newton-Raphson method for updating the density n.

3. Numerical Results

We investigate the fundamental properties of HIST equilibria in the driven or decaying λ profiles. The parameters for arbitrary functions and various computed values of HIST equilibria are shown in Tables 1 and 2, respectively. The computed various values shown in Table 2 might be in agreement with values measured on HIST. The radial driven and decaying λ profiles at the midplane are shown in Fig. 1. Both profiles are assumed on the basis of the experimental data. The driven λ profile is a hollow one, which rises up sharply near the outer edge region due to the edge drive current. The decaying λ profile is peaked one, and the position of the peak value ($R_{\rm peak}\approx0.85$) is shifted outside that of the magnetic axis ($R_{\rm axis}\approx0.65$) due to the ion flow.

The radial profiles of the magnetic structure at the midplane are shown in Fig. 2. In the driven λ profile, the toroidal field $B_{\rm t}$ has a diamagnetic profile due to the assumption $\Lambda_{\rm e}>\Lambda_{\rm i}$, and the toroidal beta value $\beta_{\rm t}$ is high

(β_t = 32%). The assumption $\Lambda_e > \Lambda_i$, which is suggested by observation in the HIST and other CHI experiments reflects that the absolute value of the electron flow velocity $\boldsymbol{u}_e$ is larger than that of the ion flow velocity $\boldsymbol{u}$. The poloidal field B_z is much smaller than B_t and is almost flat in the core region. The toroidal current density j_t has a hollow profile and is almost zero in the core region. In the decaying λ profile, B_t has a paramagnetic profile except for the inner edge region due to the assumption $\Lambda_i > \Lambda_e$, and β_t is low (β_t = 10%). The assumption $\Lambda_i > \Lambda_e$, which is suggested by observation in the HIST experiment reflects that the absolute value of $\boldsymbol{u}_e$ is smaller than that of $\boldsymbol{u}$. In addition, j_t has a centrally peaked profile with a slightly outward shift.

Table 1 Parameters for arbitrary functions

Parameters	Driven λ profile	Decaying λ profile
Λ_{i0}	0.02	0.001
Λ_{i1}	0.08	0.08
δ_{i0}	0.05	0.01
δ_{i1}	0.2	0.1
ΔY	0.2	0.02
Λ_{e0}	0.01	0.001
Λ_{e1}	0.15	0.04
δ_{e0}	0.07	0.02
δ_{e1}	0.04	0.1
$\Delta\psi$	0.02	0.02
H_{i0}	0.8	0.1
H_{i1}	1.7	1.0
δH_{i0}	0.05	0.11
δ_{Hi1}	0.07	0.25
ΔY_{Hi}	0.01	0.02
H_{e0}	0.2	0.1
H_{e1}	−2.5	0.7
δ_{He0}	0.05	0.1
δ_{He1}	0.1	0.2
$\Delta\psi_{He}$	0.08	0.02
S_{i0}	−2.0	−1.6
S_{i1}	−0.8	−1.0
δ_{Si0}	0.02	0.03
δ_{Si1}	0.07	0.06
ΔY_{Si}	0.0	0.01
S_{e0}	−2.0	−1.6
S_{e1}	−0.8	−1.2
δ_{Se0}	0.06	0.05
δ_{Se1}	0.07	0.08
$\Delta\psi_{Se}$	0.0	0.01

The radial profiles of the plasma structure at the midplane are shown in Fig. 3. In the driven λ profile, the density n profile is broad in the center. Both ion temperature T_i and electron temperature T_e have flat profiles, and their magnitudes are almost same. The electrostatic potential ϕ_E is peaked towards the peripheral region and reflects that the electric field is applied by the coaxial helicity source (CHS). In the decaying λ profile, n profile has a peak in the center with the steep gradient in the outer edge region. Similarly, both T_i and T_e have peaked profiles, and their magnitudes are almost the same. In addition, ϕ_E has almost flat profile, which reflects that the electric field is hardly applied by the CHS.

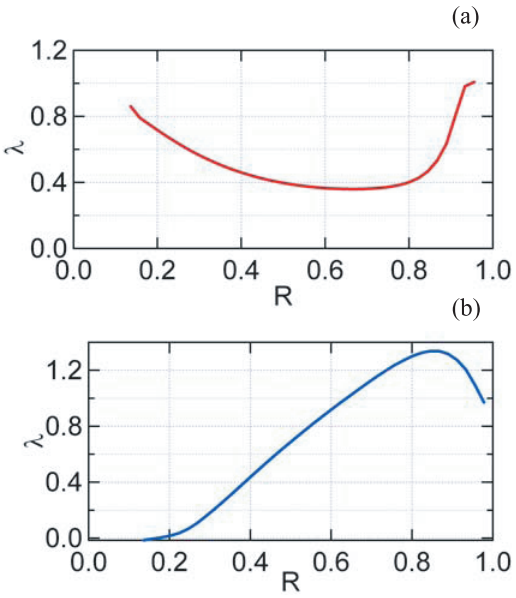

Fig. 1 Radial λ profiles at the midplane; (a) driven λ profile and (b) decaying λ profile.

Table 2 Various computed values of HIST equilibria

λ profile	Driven λ profile	Decaying λ profile
maximum value of density n_{max} [m^{-3}]	5.43×10^{19}	3.04×10^{19}
toroidal current I_t [kA]	137	64.1
poloidal current I_p [kA]	4.41	3.07
maximum value of poloidal flux $\psi_{p.max}$ [mWb]	7.85	6.26
maximum value of toroidal ion flow velocity $u_{it.max}$ [km/s]	14.5	31.7
maximum value of ion temperature $T_{i.max}$ [eV]	48.3	49.1
maximum value of electron temperature $T_{e.max}$ [eV]	56.2	42.8
toroidal beta value β_t	0.316	0.0972
volume averaged toroidal beta value $<\beta>$	0.174	0.0522

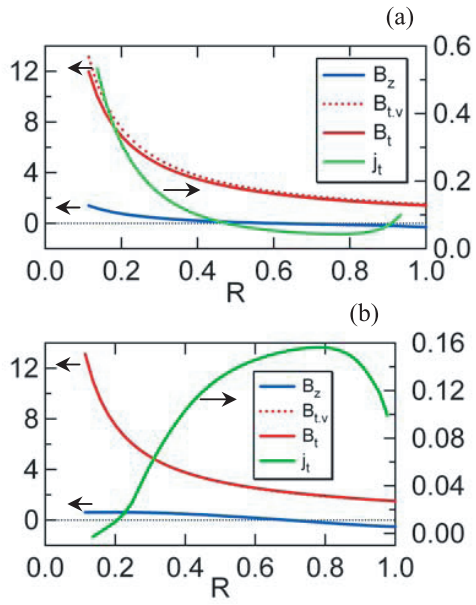

Fig. 2 Radial profiles of the magnetic field and toroidal current density at the midplane; (a) driven λ profile and (b) decaying λ profile. The blue, red dotted, red, and green lines indicate the poloidal field, vacuum toroidal field, toroidal field, and toroidal current density, respectively.

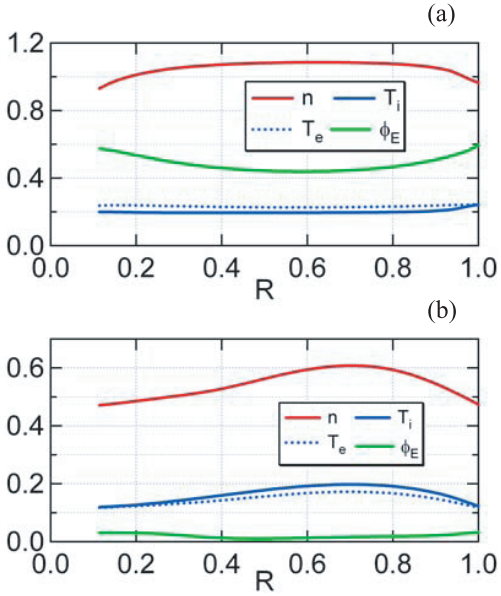

Fig. 3 Radial profiles of the density, temperature, and electrostatic potential at the midplane; (a) driven λ profile and (b) decaying λ profile. The red, blue, blue dotted, and green lines indicate the density, ion temperature, electron temperature, and electrostatic potential, respectively.

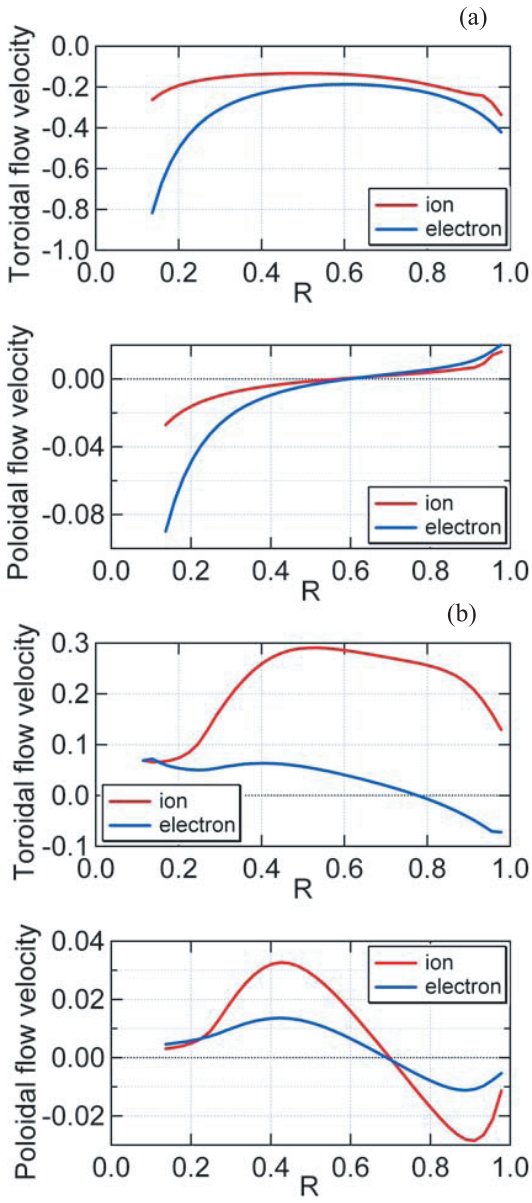

Fig. 4 Radial profiles of the toroidal and poloidal flow velocities at the midplane; (a) driven λ profile and (b) decaying λ profile. The red and blue lines indicate the ion and electron fluids, respectively.

The radial profiles of the flow structure at the midplane are shown in Fig. 4. In the driven λ profile, $\boldsymbol{u}_e$ is larger than $\boldsymbol{u}$ due to $\Lambda_e > \Lambda_i$, and $\boldsymbol{u}_e$ and $\boldsymbol{u}$ are in the same direction. Both the toroidal and poloidal electron flow velocities increase sharply near the inner edge region and cause the hollow current profile. The toroidal and poloidal currents are carried dominantly by the electron fluid in the inner edge region. The directions of the toroidal and poloidal ion flow velocities are opposite to those of the toroidal and poloidal currents, because $\boldsymbol{u}_e$ is larger than $\boldsymbol{u}$. The maximum value of the toroidal ion flow velocity ($u_{it,max} = 14.5$ km/s) and the value of the toroidal current ($I_t = 137$ kA) shown in Table 2, and the directions of the toroidal ion flow velocity u_{it} and toroidal current I_t might be in agreement with observation in the HIST and other CHI experiments. In the decaying λ profile, $\boldsymbol{u}$ is larger than $\boldsymbol{u}_e$ except for the inner edge region due to $\Lambda_i > \Lambda_e$, and u_{it} and the toroidal electron flow velocity u_{et} are in opposite directions in the outer edge region. There appears

the significant toroidal and poloidal sheared ion flows in the peripheral region. The toroidal and poloidal currents are carried dominantly by the ion fluid. The directions of u_{it} and the poloidal ion flow velocity u_{iz} are the same as those of the toroidal and poloidal currents, because $\boldsymbol{u}$ is larger than $\boldsymbol{u}_e$. The values for $u_{it.max}$ of 31.7 km/s and I_t of 64 kA are shown in Table 2, and the directions of u_{it} and I_t might be in agreement with observation in the HIST experiment. This is not enough to provide the physical interpretation of the flow velocity profiles in the driven and decaying λ cases above. However, it is difficult to specifically compare with the experimental results, because we do not have sufficient experimental results that are comparable to the theoretical results. In particularly, we have not yet measured the flow velocity profiles. Therefore, we attempt to provide the physical interpretation of the flow velocity profiles under the limited data based on the magnitudes and directions of the toroidal ion flow velocities and toroidal currents measured in the experiments.

The poloidal flux contours are shown in Fig. 5. Equilibrium configuration of the driven case is more axially elongated than that of the decaying case. The flux quantities are concentrated on the peripheral region due to the hollow current profile, and the amount of open flux is relatively large. In the case of the decaying case, the flux quantities are principally concentrated on the magnetic axis due to the centrally peaked current profile, and the amount of closed flux is large.

We show the safety factor q as a function of the normalized poloidal flux function ψ/ψ_{axis} in Fig. 6. The q profile of the driven case is almost flat. In the decaying case, the q values decrease due to the centrally peaked current

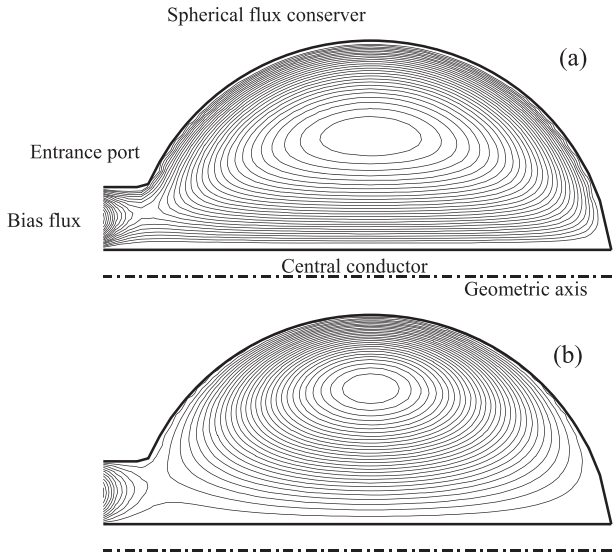

Fig. 5 Poloidal flux contours; (a) driven λ profile and (b) decaying λ profile.

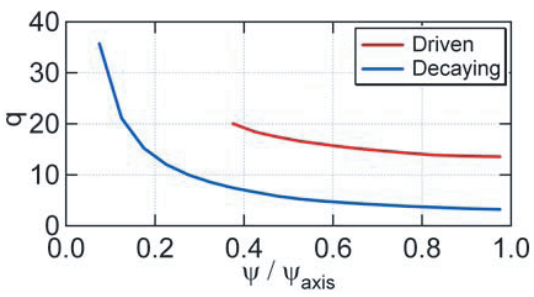

Fig. 6 Safety factor q as a function of the normalized poloidal flux function ψ/ψ_{axis}. The red and blue lines indicate the driven and decaying λ profiles, respectively.

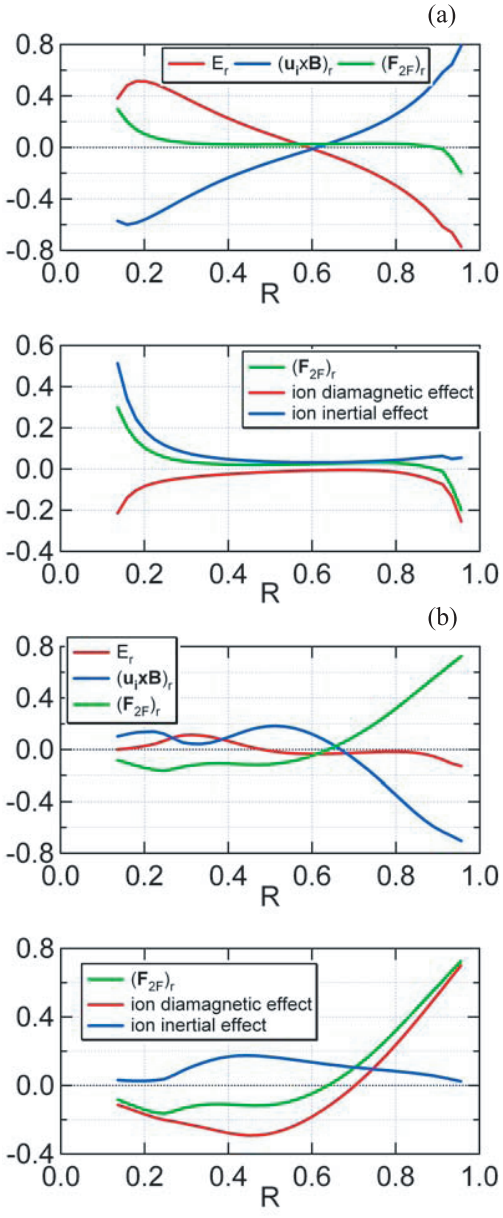

Fig. 7 Radial profiles of $\boldsymbol{E}$, $(1/\varepsilon)\boldsymbol{u}\times\boldsymbol{B}$, $\boldsymbol{F}_{2F}$, $-\nabla p_i/n$, and $-\boldsymbol{u}\cdot\nabla\boldsymbol{u}$ at the midplane; (a) driven λ profile and (b) decaying λ profile. All terms are radial components. In the upper panel of each λ profile, the red, blue, and green lines indicate $\boldsymbol{E}$, $(1/\varepsilon)\boldsymbol{u}\times\boldsymbol{B}$, and $\boldsymbol{F}_{2F}$, respectively. In the lower panel of each λ profile, the green, red, and blue lines indicate $\boldsymbol{F}_{2F}$, $-\nabla p_i/n$, and $-\boldsymbol{u}\cdot\nabla\boldsymbol{u}$, respectively.

profile, and its profile approaches the standard tokamak one. Both q profiles show values much larger than unity.

We investigate the generalized Ohm's law,

$$\boldsymbol{E} + (1/\varepsilon)\boldsymbol{u} \times \boldsymbol{B} + \boldsymbol{F}_{2\mathrm{F}} = 0,$$
$$\boldsymbol{F}_{2\mathrm{F}} = -\nabla p_{\mathrm{i}}/n - \boldsymbol{u} \cdot \nabla \boldsymbol{u}. \quad (15)$$

Here $\boldsymbol{E}$ and $\boldsymbol{F}_{2\mathrm{F}}$ express the electric field and two-fluid effects, respectively. The terms $-\nabla p_{\mathrm{i}}/n$ and $-\boldsymbol{u} \cdot \nabla \boldsymbol{u}$ cause the ion diamagnetic and inertial effects, respectively. The radial profiles of $\boldsymbol{E}$, $(1/\varepsilon)\boldsymbol{u} \times \boldsymbol{B}$, $\boldsymbol{F}_{2\mathrm{F}}$, $-\nabla p_{\mathrm{i}}/n$, and $-\boldsymbol{u} \cdot \nabla \boldsymbol{u}$ at the midplane are shown in Fig. 7. All terms are radial components. In the driven λ profile, the two-fluid effect is not large except for both the edge regions. The ion diamagnetic and inertial effects are relatively large in both the edge regions, but they are in the opposite direction. In the decaying λ profile, the two-fluid effect is dominant in the outer edge region due to the ion diamagnetic effect. In this paper, dependence of the two-fluid effect on the plasma beta is not investigated. However, Yamada *et al.* showed for uniform density plasma that the two- fluid effects are more significant for equilibria with larger two-fluid parameter ε, higher beta value, and ion flow closer to the ion diamagnetic drift [11]. Similarly, it is confirmed in our numerical results that the two-fluid effects are very important locally in the steep ion pressure region, which has a significant ion diamagnetic drift. In the future, the investigation on the dependence of the two-fluid effect on the plasma beta will be conducted for the non-uniform density plasma.

The radial profiles of the ion drift velocity at the midplane are shown in Fig. 8. All ion drift velocities are toroidal components. In the driven λ profile, the $\boldsymbol{E} \times \boldsymbol{B}$ drift velocity is dominant. This velocity has the same direction as u_{it}, but the opposite direction to I_{t}. This result is in agreement with observation in the HIST and other CHI experiments. In the decaying λ profile, the ion diamagnetic drift velocity is dominant. This velocity has the same direction as u_{it}, but the opposite direction to $\boldsymbol{E} \times \boldsymbol{B}$.

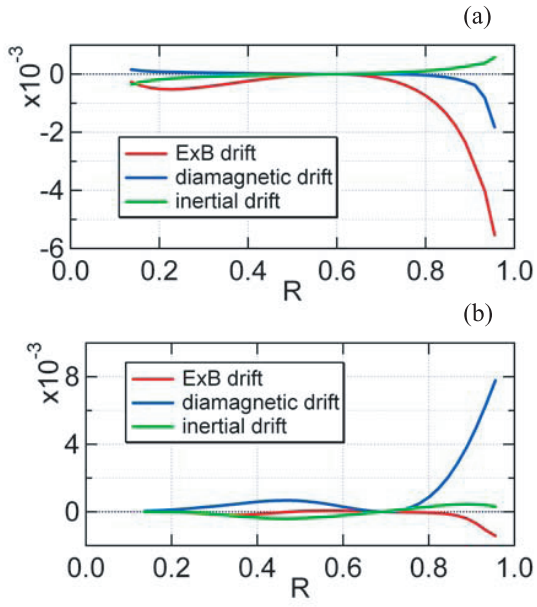

Fig. 8 Radial profiles of the ion drift velocity at the midplane; (a) driven λ profile and (b) decaying λ profile. All ion drift velocities are toroidal components. The red, blue, and green lines indicate the $\boldsymbol{E} \times \boldsymbol{B}$, diamagnetic, and inertial drift velocities, respectively.

4. Summary and Conclusions

We have computed two-dimensional two-fluid flowing equilibria with non-constant density and the poloidal as well as toroidal flows for each species by the nearby-fluids procedure. We focus our attention on the HI-ST equilibria relevant to the HIST device, which are characterized by either driven or decaying λ profiles, and explore their properties. Conclusions are summarized as follows. 1) In the driven λ profile, the equilibrium has a diamagnetic toroidal field, high-β ($\beta_{\mathrm{t}} = 32\%$), hollow current profile, and centrally broad density. The toroidal ion and electron flows are in the same direction, and two-fluid effects are less important since the $\boldsymbol{E} \times \boldsymbol{B}$ drift is dominant. 2) In the decaying λ profile, the equilibrium has a paramagnetic toroidal field, low-β ($\beta_{\mathrm{t}} = 10\%$), centrally peaked current profile, and density with a steep gradient in the outer edge region. The toroidal ion and electron flows have opposite directions in the outer edge region, and two-fluid effects are significantly locally in the edge due to the ion diamagnetic drift.

Thus far, it is difficult to compare the results of the two-fluid equilibrium computation with the experimental data completely, since several radial profiles such as the density, temperature, u_{it}, and u_{iz} are not measured yet. In the future, the measurements of these profiles will be required to verify the two-fluid effect. We have a plan to drive large flows by compact torus injection into HI-ST plasmas to investigate the effect of ion flows on the equilibrium configuration, and produce new helicity-injected two-fluid plasmas.

Acknowledgments

The authors thank Dr. Akio Ishida and Dr. Brian A. Nelson for their useful comments and discussions.

[1] K.J. McCollam and T.R. Jarboe, Plasma Phys. Control. Fusion **44**, 493 (2002).
[2] L.C. Steinhauer and A. Ishida, Phys. Rev. Lett. **79**, 3423 (1997).
[3] Z. Yoshida and S.M. Mahajan, Phys. Rev. Lett. **88**, 095001 (2002).
[4] L.C. Steinhauer, Phys. Plasmas **6**, 2734 (1999).
[5] T. Kanki and M. Nagata, Phys. Plasmas **13**, 072506 (2006).
[6] L.C. Steinhauer and A. Ishida, Phys. Plasmas **13**, 052513 (2006).
[7] M. Nagata, T. Kanki, N. Fukumoto and T. Uyama, Phys. Plasmas **10**, 2932 (2003).
[8] L. Turner, Phys. Fluids **27**, 1677 (1984).

[9] J.B. Taylor and M.F. Turner, Nucl. Fusion **29**, 219 (1989).
[10] M. Katsurai, N. Amemiya and A. Hayakawa, Kakuyugo Kenkyu **64**, 362 (1990).
[11] H. Yamada, T. Katano, K. Kanai, A. Ishida and L.C. Steinhauer, Phys. Plasmas **9**, 4605 (2002).